

Discovery of Electrochemically Induced Grain-Boundary Phase-like Transitions

Jiuyuan Nie ^{1,#}, Chongze Hu ^{1,2,#}, Qizhang Yan ¹, and Jian Luo ^{1,2,*}

¹ Department of Nanoengineering; ² Program of Materials Science and Engineering,
University of California, San Diego,
La Jolla, California 92093, U.S.A.

[#]These authors contributed equally.

^{*}Corresponding author. E-mail address: jluo@alum.mit.edu (J. Luo).

Abstract

Electric fields and currents, which are used in innovative materials processing and electrochemical energy conversion, can often alter microstructures in unexpected ways. However, little is known about the underlying mechanisms. Using ZnO-Bi₂O₃ as a model system, this study uncovers how an applied electric current can drastically change the microstructural evolution through an electrochemically induced grain boundary (GB) transition. By combining aberration-corrected electron microscopy, photoluminescence spectroscopy, first-principles calculations, a generalizable thermodynamic model, and *ab initio* molecular dynamics, this study reveals that electrochemical reduction can cause a GB disorder-to-order transition to markedly increase GB diffusivities and mobilities. Consequently, abruptly enhanced or abnormal grain growth takes place. These findings advance our fundamental knowledge of GB phase-like (complexion) transitions and electric field effects on microstructural stability and evolution, with broad scientific and technological impacts. A new method to tailor the GB structures and properties, as well as the microstructures, electrochemically can also be envisioned.

It has been long proposed¹ that grain boundaries (GBs) can be considered as two-dimensional (2D) interfacial phases (*a.k.a.* “complexions”²⁻⁷), which can undergo phase-like transitions to influence various kinetic, mechanical, chemical, electronic, ionic, and other properties^{3-5,7-12}. However, prior studies have uncovered virtually no unequivocal case of how an external stimulus – other than (a very few instances of) temperature or segregation – can induce a GB transition and subsequently alter the properties with clear underlying mechanisms. Notably, it was proposed that GB transitions can alter microstructural evolution abruptly.^{3,4,7} Also, interestingly, electric fields and currents, which are used in various innovative materials processing¹³⁻¹⁶ and electrochemical energy conversion^{17,18} and storage¹⁹ devices, can often alter microstructures unexpectedly and abruptly. However, the underlying atomic-level mechanisms remain elusive.

This study first aims at decoding how an electric field/current can alter microstructural evolution, an outstanding scientific problem of fundamental interest yet with broad technological implications. A spectrum of fascinating and intriguing observations of the “electric field effects” of suppressed^{20,21} vs. enhanced^{17,20-25} (including abnormal^{17,23}) grain growth have been made in several oxides. See Supplementary Discussion 1 for elaboration, along with a discussion of relevant materials processing technologies¹³⁻¹⁶ (including groundbreaking methods to sinter ceramics in seconds^{13,16}) where electric fields/currents can affect microstructural evolution. Moreover, electric fields and currents are present in solid oxide fuel cells^{17,18} solid-state batteries¹⁹, and various other electrochemical and electronic devices, where they can cause unexpected (often undesirable or even catastrophic) changes in microstructures or GB properties.

In a broader context, the formation and transition of 2D interfacial phases,¹ which were also named as “complexions”²⁻⁷ to differentiate them from thin layers of precipitated 3D bulk phases at GBs, can often control various materials properties.^{3-5,7-12} However, the majority of prior studies focused on symmetric tilt or twist GBs that are relatively easy to image and model. For example, a most recent study observed GB phase transitions at a symmetric tilt GB in pure copper.²⁶ General GBs (asymmetric GBs that are often of mixed tilt and twist characters²⁷) are much less understood, but they are ubiquitous and can often be the weaker links mechanically and chemically in polycrystalline materials.^{9,11,12} Moreover, Dillon and Harmer proposed that anisotropic complexion transitions at general GBs can cause the AGG,^{3,4,7} which shed light on one of the most long-standing mysteries in materials science but open questions remain. Specifically, how an

abnormal grain can initiate remains under debate for nearly a century, albeit the cause can vary for different cases.

Using ZnO-Bi₂O₃ as a model system, we uncover how an applied electric current can drastically change the microstructural evolution (including triggering AGG) through electrochemically induced phase-like transitions at general GBs. Here, we combine aberration-corrected electron microscopy, first-principles calculations, and *ab initio* molecular dynamics to reveal that electrochemical reduction can cause GB disorder-to-order transitions to markedly increase GB diffusivities. Consequently, enhanced or abnormal grain growth takes place. A generalizable thermodynamic model is further proposed. This work builds a bridge between two important areas of GB phase-like transitions and electric field effects on microstructural stability and evolution, while significantly advancing our fundamental knowledge in both areas. Furthermore, the discovery opens a new window to tailor a broad range of GB (*e.g.*, electronic or ionic) properties, as well as the microstructures, electrochemically.

ZnO-Bi₂O₃ and Characteristic Amorphous-like GBs

Here, we select Bi₂O₃-doped ZnO (with 0.5 mol% Bi₂O₃ added in the polycrystal) as our model system. The solid solubility limit of Bi₂O₃ in the ZnO crystal is <0.06 mol%²⁸ so that most Bi₂O₃ is present at GBs and triple-grain junctions.²⁹ The formation of ~0.7-0.9 nm thick liquid-like intergranular films (IGFs) at general GBs is confirmed in our reference specimen without an applied electric field by aberration-corrected scanning and high-resolution transmission electron microscopy (AC STEM and HRTEM; Fig. 1a, b and Supplementary Fig. S9). Such nanometer-thick IGFs, which have been equivalently interpreted as equilibrium-thickness liquid-like interfacial films by Clarke³⁰ or disordered multilayer adsorbates by Cannon *et al.*,³¹ represent one most widely observed complexion in ceramics.^{4,5,8,29-31} These IGFs are also called “amorphous-like” or “disordered” GBs here, albeit the existence of partial orders.^{5,6} Prior studies have demonstrated that such amorphous-like IGFs form at all general GBs in Bi₂O₃-saturated ZnO at thermodynamic equilibria both above and below the bulk eutectic temperature.²⁹ Surprisingly and interestingly, here we observe, for the first time in ZnO-Bi₂O₃, highly ordered GB structures (Fig. 1c, d, g, h).

Electrochemical Reduction Enhanced Grain Growth

We design and fabricate a Polycrystal 1/Single Crystal/Polycrystal 2 (PC1/SC/PC2) sandwich

specimen to conduct a grain growth experiment with a constant current density of 6.4 mA/mm^2 (Fig. 2a). First, we observe AGG in the PC1- region (where “-” vs. “+” denotes the reduced vs. oxidized region) near the negative electrode (cathode), as evident in Fig. 2b, c. An applied electric current can also induce similar AGG near the cathode in a simple polycrystalline specimen (Fig. 4a). Second, we observe enhanced migration of the SC/PC2- interface (Fig. 2f, g) vs. only moderate migration of the PC1+/SC interface (Fig. 2d, e). Quantitative measurements of the migration distances (shown in Supplementary Fig. S2) reveal abruptly enhanced migration at the (most reduced) middle section of the SC/PC2- interface, in comparison with the (oxidized) PC1+/SC interface and the both interfaces in a reference sandwich specimen annealed with no electric field. A detailed and quantitative comparison can be found in Supplementary Discussion 2.

Next, let us show that the PC1- and PC2- regions in our sandwich specimen (Fig. 2), where we observe increased GB mobilities (either AGG or enhanced migration of the SC/PC interface), are oxygen reduced. Here, Bi_2O_3 -enriched liquid-like IGFs in polycrystals are ion-conducting, while the ZnO single crystal is electron-conducting but ion-blocking (see Supplementary Discussion 3). Hence, PC1+ and PC2+ regions are oxidized (as the oxygen ions are blocked and accumulated near the interfaces), which is evident by the pore formation (see, *e.g.*, Fig. 2d) due to an oxidation reaction that produces O_2 . On the other hand, the PC1- and PC2- regions must be reduced (due to the depletion of oxygen ions). Subsequently, we can sketch the profiles of electric (ϕ), chemical ($\mu_{\text{O}^{2-}}$), and electrochemical ($\eta_{\text{O}^{2-}}$) potentials vs. locations in Fig. 2h according to a model presented in Supplementary Discussion 3. The electrochemical reduction in the PC1- region near the negative electrode is well expected. To prove the reduction in the PC2- region, we conduct spatially resolved photoluminescence spectroscopy to probe oxygen vacancies (Fig. 3a). The integrated photoluminescence intensities for the combined photoluminescence peak at $\sim 400\text{-}700 \text{ nm}$ (representing all defects at GBs) at different locations are shown in Fig. 3c, d. We further decompose this combined peak into a “green” band that is known to represent the oxygen vacancies and an “orange” band that most likely represents Zn interstitials (see Supplementary Discussion 4 and Fig. S8). The decomposed green-band peaks at selected locations shown in Fig. 3e, f reveal the enrichment of oxygen vacancies to prove reduction in the PC2- region (that leads to enhanced migration of the SC/PC2- interface).

Moreover, we show that the grain growth of ZnO + 0.5 mol% Bi_2O_3 polycrystals can also be enhanced in reduced atmospheres (Ar- H_2 and Ar vs. air) without an electric field (Fig. 4b-d; see

Supplementary Discussion 11). This observation further supports that the oxygen reduction (instead of the electric field) is the direct reason that promotes grain growth.

Reduction-Induced GB Disorder-Order Transitions

To probe the atomic-level mechanism of the reduction-induced increases of GB mobilities, we further examine the underlying GB structures by AC STEM (Fig. 1). On the one hand, the slow-moving oxidized PC1+/SC interface is disordered (Fig. 1e, f), similar to the characteristic amorphous-like IGFs observed in a reference specimen with no electric field (Fig. 1a, b) that also exhibits similar low mobility (see Supplementary Discussion 2). On the other hand, the fast-moving and reduced PC2-/SC interface shows highly ordered structures (Fig. 1g, h). Furthermore, the GBs of the fast-growing abnormal grains in the reduced PC1- region are also ordered (Fig. 1c, d).

The bright contrasts at GBs in the HAADF images (Fig. 1) are due to heavy Bi adsorbates (because of the *Z* contrast). Bi segregation has also been directly verified by energy dispersive X-ray spectroscopy (EDS), as shown in Supplementary Discussion 12 and Fig. S19.

Additional examples of these four cases are given in Supplementary Figs. S9-S12 to show the generality of the observations, and they are further discussed in Supplementary Discussion 5. Notably, various monolayer-, bilayer- and trilayer-like GB structures (presumably dependent on the specific crystallographic characters of the general GBs randomly selected from the specimen) have been observed in the reduced regions, but they are all ordered with high mobilities (in contrast to slow-moving amorphous-like GBs). Thus, we conclude that electrochemical reduction can generally induce disorder-to-order GB structural transitions with increased mobilities.

Fig. 5a, b further compares a pair of enlarged AC STEM high-angle annular dark-field (HAADF) images of GB structures at the oxidized PC1+/SC and the reduced SC/PC2- interfaces. Here, we also conduct image analyses to illustrate the layering and periodic orders (see Methods). While the amorphous-like GB (Fig. 5a) does show some partial orders (well-known for this type of IGFs^{5,6}), it is more disordered and wider than the reduced GB that is highly ordered and bilayer-like in the case shown in Fig. 5b.

DFT Validation of Reduction-Induced GB Transitions

Density functional theory (DFT) calculations are critically compared with AC STEM images

to further verify the reduction-induced GB disorder-to-order transition. Based on STEM images, we construct an asymmetric GB to represent a general GB for DFT calculations. We set one terminal GB plane be $(11\bar{2}0)$ to mimic both SC/PC interfaces in the STEM images (Fig. 5a, b) to build a large simulation cell of 240 atoms. We also select the Bi coverage ($\Gamma_{\text{Bi}} = \sim 11.7 \text{ nm}^{-2}$) to match prior experimental measurements²⁸ (see Methods and Supplementary Discussion 6).

DFT structural optimization shows that the stoichiometric GB (representing oxidized conditions in experiments) exhibits a more disordered structure (Fig. 5c), while a reduced GB (after removing approximately one monolayer of oxygens) exhibits a more ordered bilayer-like structure (Fig. 5d; matching the STEM image in Fig. 5b). The bilayer-like Bi adsorption can be evident in the projected Bi distribution profile shown below Fig. 5d, with the interlayer distance of $\sim 0.3 \text{ nm}$ matching the STEM measurement (Fig. 5b). Furthermore, we calculate a structural disorder parameter (η') for each atom in the DFT-relaxed structures and plot the projected disorder profiles ($\eta'(x)$) in Fig. 5e, f. For the disordered GB, the interfacial width is $\sim 0.8 \text{ nm}$ from the $\eta'(x)$ profile in Fig. 5e vs. $\sim 0.9 \text{ nm}$ from the STEM image shown in Fig. 5a (and $\sim 0.7\text{-}0.9 \text{ nm}$ for the different disordered GBs observed in this study). Further quantifications (by integrating the $\eta'(x)$ profiles) show that the stoichiometric GB has larger GB excess of disorder ($\Gamma_{\text{Disorder}} \approx 25 \text{ nm}^{-2}$) than the reduced GB ($\sim 14 \text{ nm}^{-2}$); in other words, oxygen reduction makes the GB structure more ordered, which agrees with the experiments (Fig. 5a vs. 5b).

DFT calculations have also been conducted for GBs of different levels of Bi adsorption and oxygen reduction; see Supplementary Discussion 6 for further details.

Furthermore, we calculate GB energies using the procedure described in Supplementary Discussion 8. Fig. 5g shows the DFT-computed GB energy difference $\Delta\gamma_{\text{GB}} (\equiv \gamma_{\text{GB}}^{\text{Reduced}} - \gamma_{\text{GB}}^{\text{Stoichiometric}})$, which implies a GB phase-like (complexion) transition from the disordered and stoichiometric GB to the ordered and reduced GB with decreasing oxygen chemical potential, consistent with our experimental observations.

A Generalizable Thermodynamic Model

To further discuss the physical origin of the reduction-induced GB disorder-to-order transition, we adopt a generalizable thermodynamic model following Tang *et al.*² Here, the interfacial excess grand potential for a two-component GB in a diffuse-interface model is given by:²

$$\sigma^x = \int_{-\infty}^{+\infty} \left[\Delta f(\eta, c) + \frac{\kappa_\eta^2}{2} \cdot \left(\frac{d\eta}{dx} \right)^2 + \frac{\kappa_c^2}{2} \cdot \left(\frac{dc}{dx} \right)^2 + s \cdot g(\eta) \cdot \left| \frac{d\theta}{dx} \right| \right] dx, \quad (1)$$

where concentration $c(x)$, crystallinity $\eta(x)$ ($= 1 - \eta'(x)$), and crystallographic orientation $\theta(x)$, are functions of the spatial variable x , $\Delta f(c, \eta)$ is the homogenous free energy density referenced to the equilibrium bulk phases, and κ_η , κ_c , and s are gradient energy coefficients. As derived in Supplementary Discussion 7, minimization of equation (1) leads to:

$$\sigma^x = s \cdot \Delta\theta \cdot \eta_{\text{GB}}^2 + \Delta F(\eta_{\text{GB}}), \quad (2)$$

where η_{GB} is the order parameter at the center of the GB located at $x = 0$. Here, the first term $s \cdot \Delta\theta \cdot \eta_{\text{GB}}^2$ represents an energetic penalty to have a GB misorientation $\Delta\theta$, which can be lowered by GB disordering. The second term represents the total increased free energy due to the formation of a diffuse interface, which (initially) increases with GB disordering. Thus, the equilibrium level of GB disorder, $\eta_{\text{GB}}^{\text{Equilibrium}} = 1 - \eta_{\text{GB}}^{\text{Equilibrium}}$, is determined by a tradeoff between these two terms. Specifically, equation (2) suggests that a smaller $s \cdot \Delta\theta$ will result in a more ordered GB. This is illustrated in Supplementary Fig. S15 using a graphical construction method to solve equation (2) following Cahn's critical point wetting model,³² as described in Supplementary Discussion 7.

Subsequently, we have developed a DFT-based method to estimate $s \cdot \Delta\theta$ to show that it (or s since $\Delta\theta$ is a constant) can be decreased by about 2.4 time in the reduced GB in comparison with the stoichiometric GB shown in Fig. 5; see Supplementary Discussion 7 and Table S1 for detailed derivation and calculations. Thus, the DFT calculations quantitatively justify that oxygen reduction can induce a GB disorder-to-order transition.

AIMD Simulations of Enhanced GB Diffusivities

We further perform large-scale *ab initio* molecular dynamics (AIMD) simulations to calculate and compare the GB diffusivities for the stoichiometric and reduced GBs. Fig. 5h shows the calculated GB diffusivities at 840 °C, which are increased markedly in the reduced and ordered GB in comparison with those in stoichiometric and disordered GB. Thus, the AIMD simulations suggest the increased diffusion kinetics of the reduced and ordered GBs to explain the observed increased GB mobilities.

The Intuitive Understandings of the Mechanisms

The above thermodynamic model and DFT and AIMD results can be understood intuitively. The presence of aliovalent Bi³⁺ adsorbates (substituting Zn²⁺ cations) in the stoichiometric GB likely promotes interfacial disordering. The oxygen reduction decreases the effective charge on Bi adsorbates to reduce interfacial disordering.

The differential charge density maps obtained from DFT calculations further suggest that the increased diffusivity in the reduced GB can be attributed to the weaker charge transfer and chemical bonding (see Supplementary Discussion 10). Furthermore, we calculate average Bader charges to show that the effective charge on the Bi cations is decreased with the reduction (*i.e.*, one Bi atom losses $\sim 1.4 e$ in the stoichiometric GB *vs.* $\sim 0.69 e$ in the reduced GB).

Thus, we can envision the following mechanism. The aliovalent Bi adsorbates serve as charged “hot spots” to provide “pinning” effects at the stoichiometric GB with strong charge transfer (Supplementary Fig. S17) or chemical bonding. In contrast, the oxygen reduction can reduce the effective charge on Bi adsorbates (to weaken the bonding and alleviate “pinning” effects), thereby increasing the kinetics (diffusivities and mobilities) of the reduced GB.

Summary and Perspective

In summary, ZnO-Bi₂O₃ is used as a model system to uncover a new mechanism of electrochemically induced GB transitions with significantly increased GB diffusivities, which subsequently result in enhanced and abnormal grain growth. These mechanisms have been further supported by controlled grain growth experiments and large-scale *ab initio* molecular dynamic simulations. A generalized thermodynamic model associated with DFT calculations not only shed light on the physical origin of GB disorder-to-order transition, but also enable us to forecast other materials in future studies. These findings have enriched our fundamental understandings of both electric field effects on microstructural evolution and the potentially transformative GB complexion (interfacial phase-like transition) theory via building a bridge between these two areas of great scientific importance and broad technological relevance.

Moreover, electrochemically induced GB transitions can exist in other systems and influence microstructural evolutions and various other properties, with potentially broad technological impacts on a variety of innovative materials processing technologies and electrochemical (or electronic) devices using electric fields and currents. This study also further suggests a new method to tailor the GB structure and properties electrochemically, as well as microstructures (*e.g.*, to

intentionally produce graded and far-from-equilibrium microstructures).

Methods

Preparation of polycrystal/single crystal/polycrystal (PC/SC/PC) sandwich specimens. 0.5 mol. % Bi₂O₃-doped ZnO powders were prepared by mixing ZnO (99.98% purity, ~18 nm, US Nanomaterials) with bismuth acetate ($\geq 99.99\%$ purity, Sigma Aldrich). Mixed powders were ball-milled for 10 hours with a small amount of isopropyl alcohol. Powders were subsequently dried in an oven at 80 °C for 12 hours and annealed at 500 °C for 1 hour. ZnO (11 $\bar{2}$ 0) single crystals with both sides polished were purchased from MTI Corporation (Richmond, California, USA). Dense Bi₂O₃-doped ZnO polycrystal/single crystal/polycrystal (PC/SC/PC) sandwich specimens were fabricated by spark plasma sintering (SPS) or field assisted sintering technology (FAST) at 780 °C for 5 minutes under a pressure of 50 MPa using a Thermal Technologies 3000 series SPS (Chatsworth, California, USA), and subsequently de-carbonized by annealing at 700 °C for 9 hours in air. After sintering, sandwich specimens reached >99% relative densities. Each sandwich specimen was ground to 5.0×5.0×~1.6 mm³ cuboids with a 0.5-mm thick single crystal in between, which completely separated the two polycrystalline regions.

It is worth noting that the maximum solid solubility of Bi₂O₃ in the ZnO crystal is <0.06 mol%²⁸ so that most added Bi₂O₃ (0.5 mol% in the polycrystal) is present at grain boundaries (GBs) as the liquid-like nanoscale intergranular films (see, *e.g.*, Supplementary Fig. S9) or at triple-grain junction as a minor liquid phase at the annealing temperatures of 840-880 °C (above the ZnO-Bi₂O₃ eutectic temperature of 740 °C). Nevertheless, we adopt the term “Bi₂O₃-doped ZnO” that is commonly used in the ceramics field, albeit we acknowledge the majority of Bi is not doped into the ZnO crystal lattice.

Annealing with an applied electric current. Dense PC/SC/PC sandwich specimens were sputtered with platinum to form electrodes on both sides of two polycrystalline regions using a Denton Discover 18 Sputter (Moorestown, New Jersey, USA). An external DC electric current was applied on the specimen while annealing at a furnace temperature of 840 °C for 4 hours and maintaining a constant DC current density of $J = 6.4 \text{ mA/mm}^2$. The specimen temperature, which was higher than the furnace temperature due to the Joule heating, was estimated to be ~865 °C based on the electric power density and radiation heat transfer using a method described previously.²² The electric field direction was perpendicular to the imbedded ZnO (11 $\bar{2}$ 0) single crystal. More details of the experimental setup can be found in a prior publication (where the same setup was used for flash sintering experiments).³³ All specimens were air quenched for characterization.

Annealing experiments without an electric field/current. To rule out the effects of the Joule heating with the applied electric current (that heated the specimen up by ~25 °C), the reference sandwich specimen was annealed at 880 °C for 4 hours using the exact same experimental setup but without any external electric field/current (*i.e.*, 40 °C higher in comparison with the furnace temperature of 840 °C for the specimen annealed with the applied electric current). As we noted in the prior section, the specimen temperature was estimated to be ~865 °C based on the Joule heating and radiation heat transfer²² for the specimen annealed with the applied electric current. Thus, the annealing temperature of the reference specimen was (intentionally set to be) above the upper limit of the estimated specimen temperature of the case with an applied electric current. This ensures that any increased GB mobilities observed in the specimen with the applied electric current was not due to thermal effects (Joule heating).

The reference PC/SC/PC sandwich specimens were examined before and after the isothermal annealing (without an applied electric field/current), and the relevant SEM cross-sectional images are shown in Supplementary Fig. S6 and Fig. S7, respectively.

In addition, three dense polycrystalline specimens were prepared by using the same condition described above, and subsequently annealed at 880 °C for 4 hours without electric field/current in air, Ar, and Ar +

5% H₂, respectively, to investigate the effects of reducing atmospheres on grain growth. The results shown in Fig. 4b-d and Supplementary Fig. S18 further confirm that oxygen reduction can enhance grain growth.

After isothermal annealing, all specimens were air quenched for characterization.

Characterization of microstructures and grain growth. The densities of sandwich specimens were measured using the Archimedes method. Quenched specimens were characterized by using an ultra-high-resolution scanning electron microscope (Apreo SEM, FEI, Hillsboro, Oregon, USA) on the cross sections after grinding and polishing. Electron backscatter diffraction (EBSD) mapping was acquired by using an c-wave detector from Oxford Instruments (Concord, MA, USA).

The growth of the single crystal front was measured at 14 locations ($\times 16$ measurements per location) along each polycrystal-single crystal (PC/SC) interface for each case. At each location, the migration of the single crystal front (of the PC/SC interface) was averaged from 16 individual measurements with 5 μm intervals. The measured were conducted for both PC/SC interfaces in the specimens annealed with and without an applied electric field (for four cases all together). The results are plotted in Supplementary Fig. S2.

Photoluminescence spectroscopy. Spatially resolved photoluminescence spectroscopy in the wavelength range from 400 nm to 700 nm on the cross-sectional surface of the sandwich specimen was carried out on a confocal microscope (Leica SP5, Leica Microsystems, Wetzlar, Germany) equipped with a multiphoton system. The microscope spatial resolution is $\sim 0.4 \mu\text{m}$, and the penetration depth is $\sim 50 \text{ nm}$.

Aberration-corrected electron microscopy and energy dispersive X-ray spectroscopy. Transmission electron microscopy (TEM) samples were prepared by using a dual-beam focused ion beam (FIB) / SEM system (Scios, FEI, Hillsboro, Oregon, USA) to lift out specimens of the selected GBs from the cross section based on the EBSD and SEM images.

Aberration-corrected scanning transmission electron microscopy characterization (AC STEM) of the GB structures was conducted by using a JEOL JEM-300CF STEM microscope (Akishima, Tokyo, Japan) operating at 300 kV. Both high-angle annular dark-field (HAADF) and bright field (BF) images were recorded.

Energy dispersive X-ray spectroscopy (EDS) was used in conjunction with STEM to confirm segregated regions (the GB complexions observed by STEM with bright contrast in HAADF imaging) are Bi-enriched (Supplementary Fig. S19).

STEM image analyses to reveal order/disorder. To examine the order and disorder (including the partial order in the amorphous-like GBs), we conducted two types of image analyses of the STEM images to reveal the layering *vs.* lateral orders, as follows.

First, we integrated the STEM HAADF intensities along the direction parallel to the GB to show the layering orders. Two examples of an amorphous-like GB (IGF) *vs.* an ordered bilayer are plotted as the yellow lines on the top of the STEM images in Fig. 5a, b.

Second, we conducted line-by-line fast Fourier transition (FFT) analysis to probe the lateral periodic orders. Here, we selected a rectangular frame (with the width being equal to the lattice spacing), moved the frame pixel by pixel, and conducted “line-by-line FFT analysis” of the crystalline order. Examples of an amorphous-like GB (IGF) *vs.* an ordered bilayer are plotted at the bottom panels in Fig. 5a, b.

First-principles density functional theory (DFT) calculations. The GBGenerator³⁴ code in Python Materials Genomics (pymatgen) library³⁵ was used to construct ZnO GB structure. The lattice parameters of the ZnO hexagonal structure ($a = 3.29 \text{ \AA}$ and $c = 5.31 \text{ \AA}$) were taken from the Materials Project³⁶.

An asymmetric GB terminated by $(11\bar{2}0)$ plane (the two GBs shown in Fig. 5a, b) always requires a large simulation cell. Thus, we select the other GB plane to be the non-polar $(10\bar{1}0)$ with a rotate angle of $\sim 53^\circ$ along the $[100]$ axis to construct a feasible model to mimic the GBs observed in the experiments (Fig. 5) within the limitation of the DFT cell size. Since lattice matching conditions cannot be achieved in three directions to apply periodic boundary conditions, a 15 \AA thick layer of vacuum was added to isolate the interaction between two free surfaces created. The final simulation cell is triclinic with parameters: $a = 0.62 \text{ nm}$, $b = 1.45 \text{ nm}$, $c = 5.30 \text{ nm}$, $\alpha = 104.69^\circ$, $\beta = 78.69^\circ$, and $\gamma = 74.70^\circ$. This simulation cell contains 240 atoms in total, which is about the largest for effective DFT and AIMD simulations.

The first-principles DFT calculations were performed by using the Vienna *ab initio* Simulations Package (VASP)^{37,38}. The Kohn-Sham equations were used to solve the projected-augmented wave (PAW) method^{39,40} along with standard PAW potentials for the elements Zn, O, and Bi. The Perdew-Burke-Ernzerhof (PBE)⁴⁰ exchange-correlation functional was utilized to perform the structural optimization for the GB structure. The lattice parameters of ZnO were kept unchanged during the relaxation and only atomic positions were subjected to relaxation. All atoms were fully relaxed until the Hellmann-Feynman forces were smaller than 0.02 eV/\AA . The Brillouin-zone integrations were sampled on a Γ -centered $4 \times 2 \times 1$ k -point grids. The kinetic energy cutoff for plane waves was set to 400 eV . The convergence criterion for electronic self-consistency was adopted to 10^{-4} eV .

Quantification of GB order/disorder from DFT simulations. A bond-orientational order parameter η was calculated for each atom⁴¹. Subsequently, we defined a dimensionless disorder parameter ($\eta' \equiv 1 - \eta$; $\eta' = 1$ for an atom in a liquid and $\eta' = 0$ for an atom in a perfect crystal).

The 1D distribution of disorder parameter $\eta'(x)$ was obtained by averaging the η' values of atoms in the directions parallel to the GB plane. Two examples of disorder parameter profiles $\eta'(x)$ for the amorphous-like GB (IGF) vs. the ordered bilayer are shown in Fig. 5e, f. Subsequently, GB excess disorder was quantified by integrating the disorder profile $\eta'(x)$. More details can be found in prior publications where similar analyses were performed for atomistic simulations using empirical potentials^{9,42,43} (vs. extending the definitions and methodologies to DFT relaxed GB structures here in this study).

Quantification of atomic density profiles from DFT simulations. We used a coarse-grained method to compute 1D atomic density profiles from DFT-relaxed GB structures to compare with the STEM results. In this procedure⁹, a Gaussian function was assigned to each atom and the overall density distribution function can be computed by summing all Gaussian functions. Two examples of Bi profiles for the amorphous-like GB vs. the ordered bilayer are shown in Fig. 5c, d.

***Ab initio* molecular dynamics (AIMD) simulations of GB diffusivities.** Based on the optimized GB structures, we performed *ab initio* molecular dynamics (AIMD) simulations under the *NVT* ensemble with a Nose-Hoover thermostat^{44,45} to obtain GB diffusivities. The temperature was set to 1123 K (850°C), close to the experimental annealing condition. The overall simulation time was set to 1500 fs with a time step of 1 fs . Although the overall simulation time is relatively short (due to the limitation of a very large simulation cell), we believe the GB structures can achieve equilibrium based on monitoring the potential energy vs. time. The k -point grids were adopted to $1 \times 1 \times 1$ (Γ point only). To avoid the effects of vacuum, we fixed 2~3 monolayer atoms near the free surfaces and only allowed other atoms to move. The atoms' trajectories during AIMD simulation were used to calculate the mean square displacement (MSD) over time (t). Finally, the GB diffusivities for Zn, O and Bi, respectively, were obtained by linearly fitting the corresponding MSD vs. t curves for both stoichiometric and reduced GBs for comparison (Fig. 5h).

Data availability

All data are available from the corresponding authors on reasonable request.

References:

- 1 Hart, E. W. 2-dimensional phase transformation in grain boundaries. *Scripta Metallurgica* **2**, 179-&, doi:10.1016/0036-9748(68)90222-6 (1968).
- 2 Tang, M., Carter, W. C. & Cannon, R. M. Grain boundary transitions in binary alloys. *Physical Review Letters* **97**, 075502 (2006).
- 3 Dillon, S. J., Tang, M., Carter, W. C. & Harmer, M. P. Complexion: A new concept for kinetic engineering in materials science. *Acta Materialia* **55**, 6208-6218, doi:10.1016/j.actamat.2007.07.029 (2007).
- 4 Cantwell, P. R. *et al.* Grain boundary complexions. *Acta Materialia* **62**, 1-48, doi: 10.1016/j.actamat.2013.07.037 (2014).
- 5 Kaplan, W. D., Chatain, D., Wynblatt, P. & Carter, W. C. A review of wetting versus adsorption, complexions, and related phenomena: The rosetta stone of wetting *Journal of Materials Science* **48**, 5681-5717 (2013).
- 6 Baram, M., Chatain, D. & Kaplan, W. D. Nanometer-thick equilibrium films: The interface between thermodynamics and atomistics. *Science* **332**, 206-209 (2011).
- 7 Cantwell, P. R. *et al.* Grain boundary complexion transitions. *Annual Review of Materials Research* **50** (2020).
- 8 Luo, J. Stabilization of nanoscale quasi-liquid interfacial films in inorganic materials: A review and critical assessment. *Critical Reviews in Solid State and Materials Sciences* **32**, 67-109, doi:10.1080/10408430701364388 (2007).
- 9 Hu, T., Yang, S., Zhou, N., Zhang, Y. & Luo, J. Role of disordered bipolar complexions on the sulfur embrittlement of nickel general grain boundaries. *Nature Communications* **9**, 2764, doi:10.1038/s41467-018-05070-2 (2018).
- 10 Luo, J. Let thermodynamics do the interfacial engineering of batteries and solid electrolytes. *Energy Storage Materials* **21**, 50-60, doi:10.1016/j.ensm.2019.06.018 (2019).
- 11 Yu, Z. *et al.* Segregation-induced ordered superstructures at general grain boundaries in a nickel-bismuth alloy. *Science* **358**, 97-101, doi:10.1126/science.aam8256 (2017).
- 12 Luo, J., Cheng, H., Asl, K. M., Kiely, C. J. & Harmer, M. P. The role of a bilayer interfacial phase on liquid metal embrittlement. *Science* **333**, 1730-1733 (2011).
- 13 Cologna, M., Rashkova, B. & Raj, R. Flash sintering of nanograin zirconia in <5 s at 850°C. *Journal of the American Ceramic Society* **93**, 3556-3559, doi:10.1111/j.1551-2916.2010.04089.x (2010).
- 14 Kim, S.-W., Kang, S.-J. L. & Chen, I. W. Electro-sintering of yttria-stabilized cubic zirconia. *Journal of the American Ceramic Society* **96**, 1398-1406, doi:10.1111/jace.12291 (2013).
- 15 Munir, Z. A., Anselmi-Tamburini, U. & Ohyanagi, M. The effect of electric field and pressure on the synthesis and consolidation of materials: A review of the spark plasma sintering method. *Journal of Materials Science* **41**, 763-777, doi:10.1007/s10853-006-6555-2 (2006).
- 16 Wang, C. *et al.* A general method to synthesize and sinter bulk ceramics in seconds. *Science* **368**, 521-526, doi:10.1126/science.aaz7681 (2020).
- 17 Dong, Y. & Chen, I. W. Oxygen potential transition in mixed conducting oxide electrolyte. *Acta Materialia* **156**, 399-410, doi:10.1016/j.actamat.2018.06.014 (2018).
- 18 Sierra, J. *et al.* In-operando observation of microstructural evolution in a solid oxide cell electrolyte operating at high polarization. *Journal of Power Sources* **413**, 351-359 (2019).
- 19 Tian, H.-K., Liu, Z., Ji, Y., Chen, L.-Q. & Qi, Y. Interfacial electronic properties dictate Li dendrite growth in solid electrolytes. *Chemistry of Materials* **31**, 7351-7359 (2019).

- 20 Conrad, H. & Yang, D. Dependence of the sintering rate and related grain size of yttria-stabilized polycrystalline zirconia (3Y-TZP) on the strength of an applied dc electric field. *Mater. Sci. Eng. A* **528**, 8523-8529, doi:10.1016/j.msea.2011.08.022 (2011).
- 21 Yang, D. & Conrad, H. Enhanced sintering rate of zirconia (3Y-TZP) by application of a small ac electric field. *Scripta Materialia* **63**, 328-331, doi:10.1016/j.scriptamat.2010.04.030 (2010).
- 22 Zhang, Y., Jung, J.-I. & Luo, J. Thermal runaway, flash sintering and asymmetrical microstructural development of ZnO and ZnO–Bi₂O₃ under direct currents. *Acta Materialia* **94**, 87-100, doi: 10.1016/j.actamat.2015.04.018 (2015).
- 23 Kim, S. W., Kim, S. G., Jung, J. I., Kang, S. J. L. & Chen, I. W. Enhanced grain boundary mobility in yttria-stabilized cubic zirconia under an electric current. *Journal of the American Ceramic Society* **94**, 4231-4238, doi:10.1111/j.1551-2916.2011.04800.x (2011).
- 24 Rheinheimer, W., Füllung, M. & Hoffmann, M. J. Grain growth in weak electric fields in strontium titanate: Grain growth acceleration by defect redistribution. *Journal of the European Ceramic Society* **36**, 2773-2780, doi:10.1016/j.jeurceramsoc.2016.04.033 (2016).
- 25 Zhang, Y., Nie, J. & Luo, J. Flash sintering activated by bulk phase and grain boundary complexion transformations. *Acta Materialia* **181**, 544-554, doi:10.1016/j.actamat.2019.10.009 (2019).
- 26 Meiners, T., Frolov, T., Rudd, R. E., Dehm, G. & Liebscher, C. H. Observations of grain-boundary phase transformations in an elemental metal. *Nature* **579**, 375-378 (2020).
- 27 Morawiec, A. & Glowinski, K. On “macroscopic” characterization of mixed grain boundaries. *Acta materialia* **61**, 5756-5767 (2013).
- 28 Lee, J.-R., Chiang, Y.-M. & Ceder, G. Pressure-thermodynamic study of grain boundaries: Bi segregation in ZnO. *Acta Materialia* **45**, 1247-1257 (1997).
- 29 Chiang, Y.-M., Wang, H. & Lee, J.-R. Hrem and stem of intergranular films at zinc oxide varistor grain boundaries. *Journal of Microscopy* **191**, 275-285 (1998).
- 30 Clarke, D. R. On the equilibrium thickness of intergranular glass phases in ceramic materials. *Journal of the American Ceramic Society* **70**, 15-22 (1987).
- 31 Cannon, R. M. *et al.* Adsorption and wetting mechanisms at ceramic grain boundaries. *Ceramic Transactions (Grain Boundary Engineering in Ceramics)* **118**, 427-444 (2000).
- 32 Cahn, J. W. Critical point wetting. *Journal of Chemical Physics* **66**, 3667-3672 (1977).
- 33 Zhang, Y., Nie, J., Chan, J. M. & Luo, J. Probing the densification mechanisms during flash sintering of zno. *Acta Materialia* **125**, 465-475, doi:j.actamat.2016.12.015 (2017).
- 34 Zheng, H. *et al.* Grain boundary properties of elemental metals. *Acta Materialia* **186**, 40-49, doi: j.actamat.2019.12.030 (2020).
- 35 Ong, S. P. *et al.* Python materials genomics (pymatgen): A robust, open-source python library for materials analysis. *Computational Materials Science* **68**, 314-319, doi: j.commsci.2012.10.028 (2013).
- 36 Jain, A. *et al.* Commentary: The materials project: A materials genome approach to accelerating materials innovation. *APL Materials* **1**, 011002, doi:10.1063/1.4812323 (2013).
- 37 Kresse, G. & Furthmüller, J. Efficient iterative schemes for ab initio total-energy calculations using a plane-wave basis set. *Physical Review B* **54**, 11169-11186, doi:10.1103/PhysRevB.54.11169 (1996).
- 38 Kresse, G. & Hafner, J. Ab initio molecular dynamics for liquid metals. *Physical Review B* **47**, 558-561, doi:10.1103/PhysRevB.47.558 (1993).
- 39 Blöchl, P. E. Projector augmented-wave method. *Physical Review B* **50**, 17953-17979, doi:10.1103/PhysRevB.50.17953 (1994).
- 40 Perdew, J. P., Burke, K. & Ernzerhof, M. Generalized gradient approximation made simple. *Physical Review Letters* **77**, 3865-3868, doi:10.1103/PhysRevLett.77.3865 (1996).

- 41 Chua, A. L., Benedek, N. A., Chen, L., Finnis, M. W. & Sutton, A. P. A genetic algorithm for predicting the structures of interfaces in multicomponent systems. *Nature Materials* **9**, 418 (2010).
- 42 Hu, C., Zuo, Y., Chen, C., Ping Ong, S. & Luo, J. Genetic algorithm-guided deep learning of grain boundary diagrams: Addressing the challenge of five degrees of freedom. *Materials Today*, doi: j.mattod.2020.03.004 (2020).
- 43 Yang, S., Zhou, N., Zheng, H., Ong, S. P. & Luo, J. First-order interfacial transformations with a critical point: Breaking the symmetry at a symmetric tilt grain boundary. *Physical review letters* **120**, 085702 (2018).
- 44 Evans, D. J. & Holian, B. L. The nose–hoover thermostat. *The Journal of Chemical Physics* **83**, 4069-4074, doi:10.1063/1.449071 (1985).
- 45 Deng, Z., Zhu, Z., Chu, I.-H. & Ong, S. P. Data-driven first-principles methods for the study and design of alkali superionic conductors. *Chemistry of Materials* **29**, 281-288, doi:10.1021/acs.chemmater.6b02648 (2017).
- 46 Hofmann, D. M. *et al.* Properties of the oxygen vacancy in ZnO. *Applied Physics A* **88**, 147-151, doi:10.1007/s00339-007-3956-2 (2007).
- 47 Auret, F. D., Goodman, S. A., Legodi, M. J., Meyer, W. E. & Look, D. C. Electrical characterization of vapor-phase-grown single-crystal zno. *Applied Physics Letters* **80**, 1340-1342, doi:10.1063/1.1452781 (2002).
- 48 Van de Walle, C. G. Defect analysis and engineering in ZnO. *Physica B: Condensed Matter* **308-310**, 899-903, doi: 10.1016/S0921-4526(01)00830-4 (2001).
- 49 Luo, J., Wang, H. & Chiang, Y.-M. Origin of solid-state activated sintering in Bi₂O₃-doped ZnO. *Journal of the American Ceramic Society* **82**, 916-920, doi:10.1111/j.1151-2916.1999.tb01853.x (1999).
- 50 Wang, H. & Chiang, Y.-M. Thermodynamic stability of intergranular amorphous films in bismuth-doped zinc oxide. *Journal of the American Ceramic Society* **81**, 89-96 (1998).
- 51 Tang, M., Carter, W. C. & Cannon, R. M. Grain boundary order-disorder transitions. *Journal of Materials Science* **41**, 7691-7695 (2006).

Acknowledgments: This work is supported by the Aerospace Materials for Extreme Environments program of the U.S. Air Force Office of Scientific Research (AFOSR) under the grants nos. FA9550-14-1-0174 and FA9550-19-1-0327.

Author contributions: J. L. conceived the idea and supervised the work. J. N. conducted most experiments and Q. Y assisted some experiments and data analysis. C.H. performed DFT calculations and AIMD simulations. All authors drafted, reviewed, and revised the manuscript.

Competing interests: The authors declare no conflict of interests.

Supplementary Information:

Supplementary Discussions 1 to 12
Supplementary Tables S1-S2
Supplementary Figures S1 to S20
Supplementary References

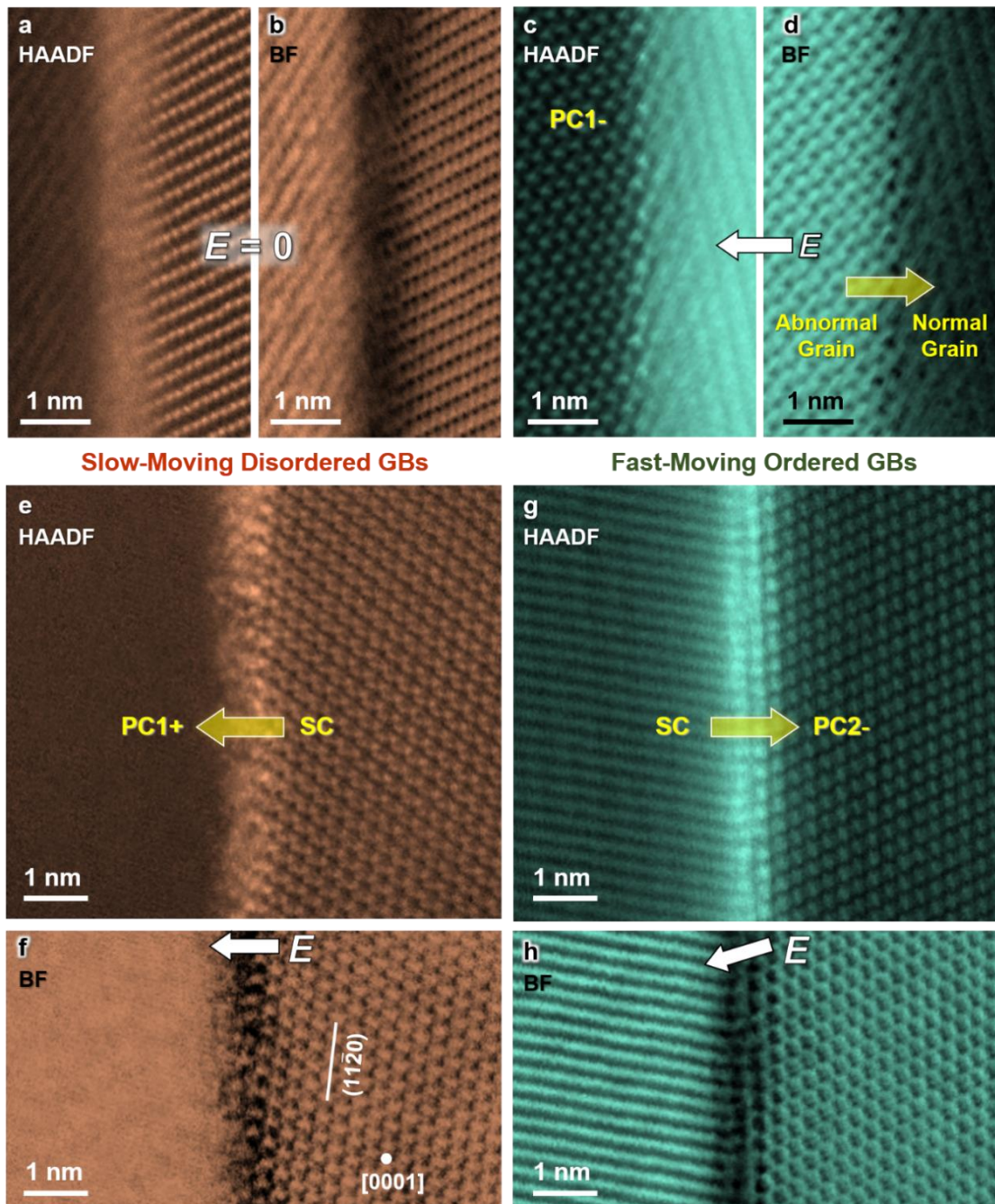


Fig. 1 AC STEM high-angle annular dark-field (HAADF) and bright-field (BF) images of representative slow-moving disordered vs. fast-moving ordered GBs. **a, b,** A nanoscale amorphous-like IGF (*a.k.a.* disordered GB) observed in a reference specimen annealed without an electric field, which is characteristic of all general GBs in Bi_2O_3 -saturated ZnO .²⁹ STEM images of **(c, d)** an ordered GB of an abnormal grain in the electrochemically reduced PC1- region, as well as **(e, f)** a slow-moving disordered GB at the oxidized PC1+/SC interface vs. **(g, h)** a fast-moving ordered GB at the reduced SC/PC2- interface in a PC1/SC/PC2 sandwich specimen annealed with an applied electric current (as schematically shown in Fig. 2a). STEM images for additional examples can be found in Supplementary Figs. S9-S12, showing the generality of the observations of slow-moving disordered GBs vs. fast-moving ordered GBs.

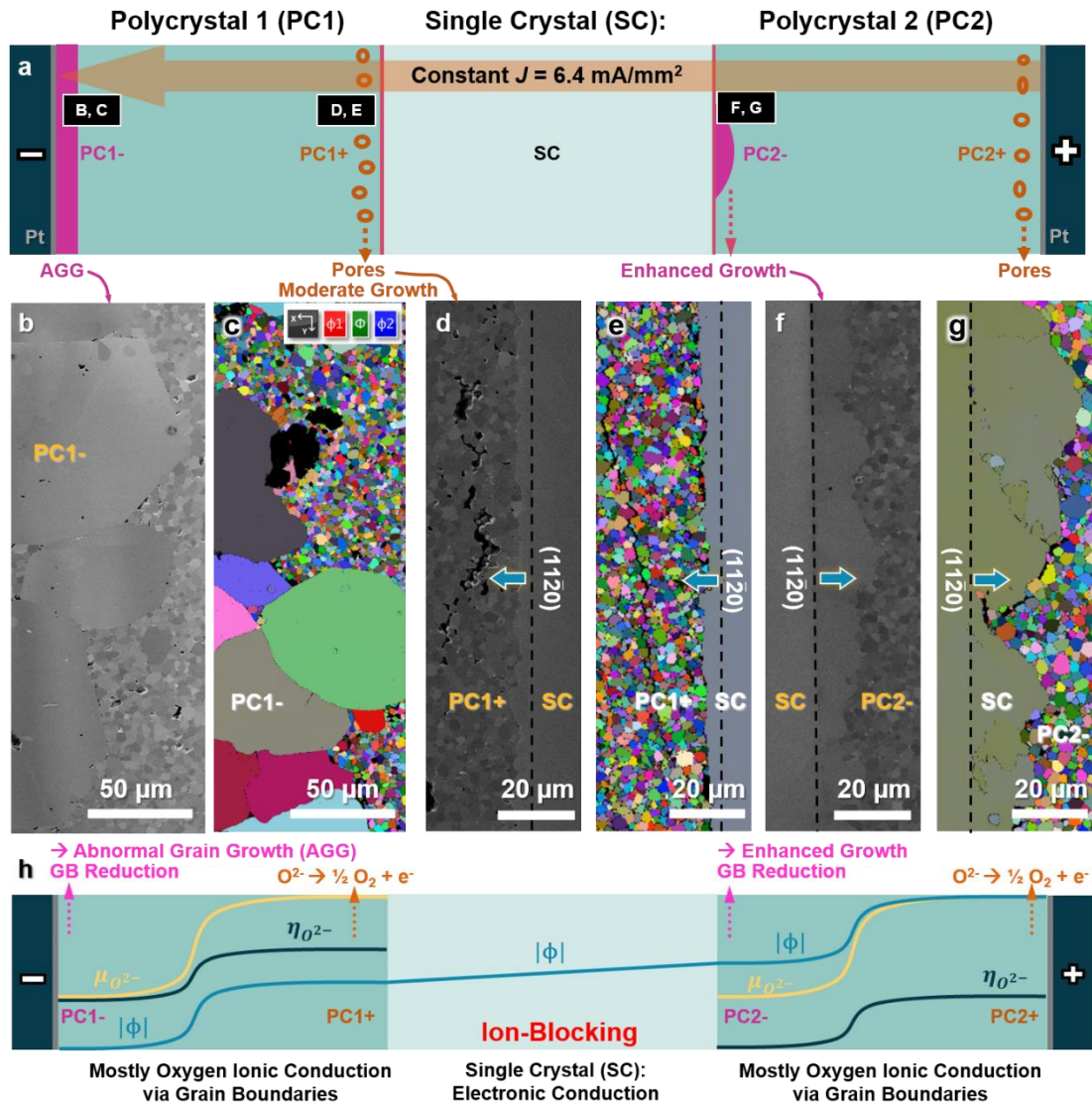


Fig. 2 Microstructure of a Bi_2O_3 -doped ZnO sandwich specimen isothermally annealed under a constant applied current. **a**, A schematic illustration of this PC1/SC/PC2 sandwich specimen. Enhanced or abnormal grain growth takes place in the reduced PC1- and PC2- regions. Cross-sectional scanning electron microscopy (SEM) micrographs and electron backscatter diffraction (EBSD) Euler maps of **(b, c)** abnormal grain growth (AGG) near the cathode in the reduced PC1- region, as well as **(d, e)** moderate migration of the oxidized PC1+/SC interface vs. **(f, g)** enhanced migration of the reduced SC/PC2- interface. Dashed lines indicate the original positions of the SC/PC interfaces. See Supplementary Fig. S2 for quantitative measurements of migration distances of both PC1+/SC and SC/PC2- interfaces (in comparison with those in a reference sandwich specimen without an applied electric field) and Supplementary Figs. S3-S5 for additional EBSD maps. **h**, Schematic profiles of electric (ϕ), chemical ($\mu_{O^{2-}}$), and electrochemical ($\eta_{O^{2-}}$) potentials vs. locations. See Supplementary Fig. S1 for further detail.

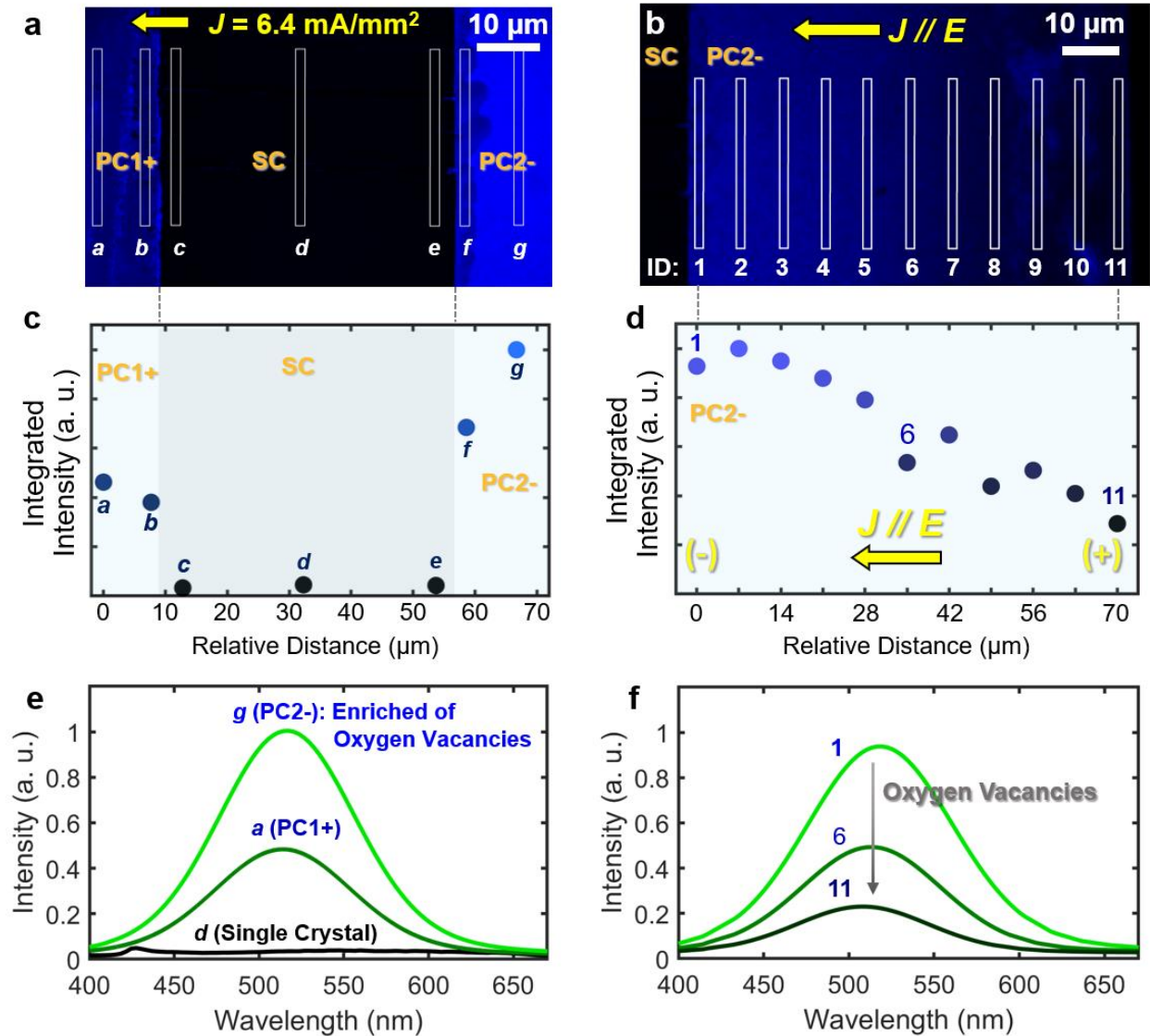


Fig. 3 Photoluminescence spectroscopy of the sandwich specimen annealed with a constant applied electric current, suggesting the enrichment of oxygen vacancies in the reduced PC2- region. **a, b**, Maps of the photoluminescence intensity at the 526 nm wavelength of the cross-sectional PC1/SC/PC2 sandwich specimen. **c, d**, Integrated photoluminescence intensities for the combined photoluminescence peak at $\sim 400\text{-}700 \text{ nm}$ at different locations, representing all defects at GBs. Photoluminescence spectra are collected at Locations *a-g* labeled in Panel (a) and Locations 1-11 labeled in Panel (b), respectively. **e, f**, The photoluminescence intensity vs. wavelength curves of decomposed green-emission band (representing the oxygen vacancy concentration) at selected locations. See Supplementary Discussion 4 and Fig. S8 for further detail.

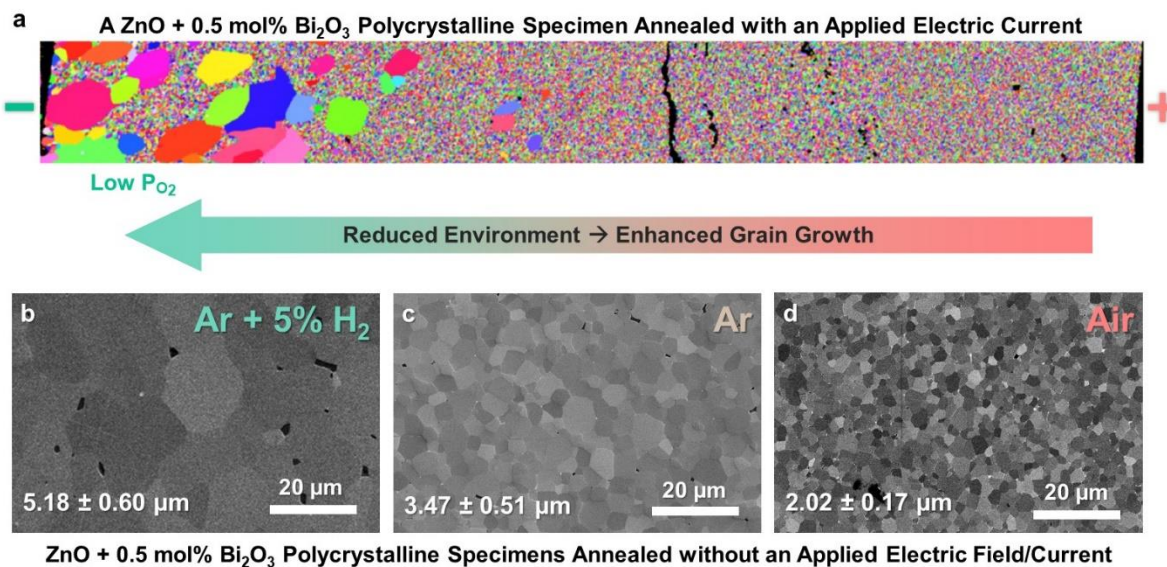


Fig. 4 Enhanced grain growth in reduced environments for ZnO + 0.5 mol% Bi₂O₃ polycrystalline specimens. **a**, EBSD map of a ZnO + 0.5 mol% Bi₂O₃ polycrystalline specimen (without a single-crystal section) annealed with an applied current, showing similar abnormal grain growth in the reduced region near the cathode (negative electrode). Cross-sectional SEM micrographs of polycrystalline specimens quenched from 880°C after annealing for 4 hours in **b**, Ar + 5% H₂ **c**, Ar, and **d**, air. Additional low-magnification images are shown in Supplementary Fig. S18. These observations further support that the oxygen reduction caused enhanced grain growth.

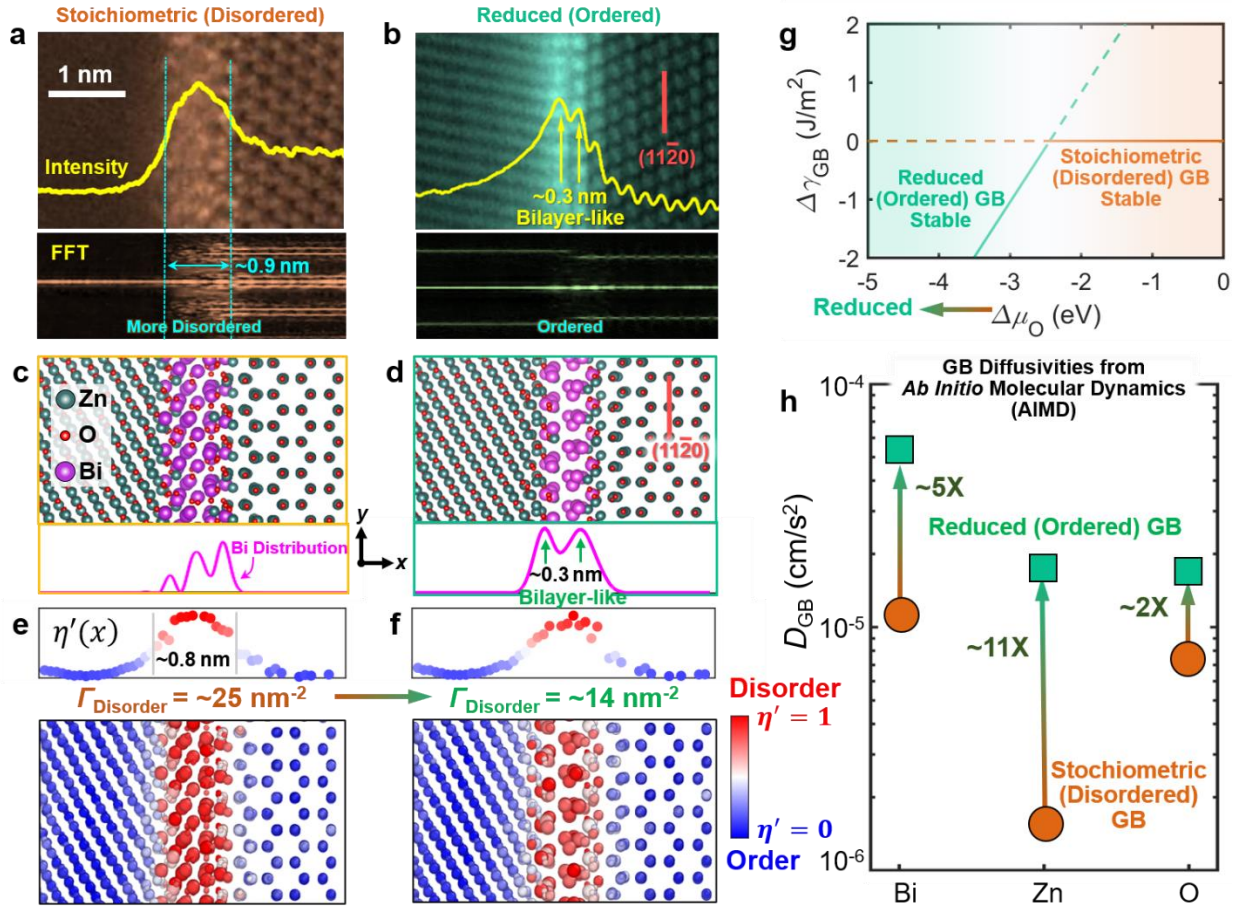


Fig. 5 Comparison of experiments and DFT simulations of stoichiometric (disordered) vs. reduced (ordered) GB structures and AIMD simulated GB diffusivities. Expanded experimental STEM HAADF images for (a) a disordered stoichiometric GB vs. (b) an ordered (bilayer-like) reduced GB; here, we plot the averaged HAADF intensity and line-by-line FFT patterns to illustrate the layering and periodic orders. DFT-optimized structures of (c) the stoichiometric vs. (d) reduced GBs, where the projected Bi density profiles are plotted beneath. The calculated disorder parameters for all atoms for DFT-optimized (e) stoichiometric vs. (f) reduced GB structures. The projected disorder parameter profiles ($\eta'(x)$) are shown above. The GB excess of disorder (computed by integrating $\eta'(x)$) decreases from $\Gamma_{\text{Disorder}} = \sim 25 \text{ nm}^{-2}$ for the stoichiometric GB to $\Gamma_{\text{Disorder}} = \sim 14 \text{ nm}^{-2}$ for the reduced GB, thereby showing that the oxygen reduction induces GB ordering. **g**, Computed GB energy difference $\Delta\gamma_{\text{GB}} (\equiv \gamma_{\text{GB}}^{\text{Reduced}} - \gamma_{\text{GB}}^{\text{Stoichiometric}})$ vs. oxygen chemical potential difference $\Delta\mu_{\text{O}} (\equiv \mu_{\text{O}} - \frac{1}{2}E_{\text{O}_2})$, showing a transition from the stoichiometric (disordered) GB to the reduced (ordered) GB with decreasing oxygen chemical potential, consistent with experiments. **h**, GB diffusivities calculated by AIMD simulations. The GB diffusivities in the reduced (ordered) GB are markedly increased in comparison with those in the stoichiometric (disordered) GB.